CHINESE OPTICS LETTERS

Vol. 21, No. 3 | March 2023

Advances in multipass cell for absorption spectroscopy-based trace gas sensing technology [Invited]

Yahui Liu (刘亚辉) and Yufei Ma (马欲飞)*

National Key Laboratory of Science and Technology on Tunable Laser, Harbin Institute of Technology, Harbin 150001, China

*Corresponding author: mayufei@hit.edu.cn

Received September 19, 2022 | Accepted November 7, 2022 | Posted Online December 1, 2022

In the field of absorption spectroscopy, the multipass cell (MPC) is one of the key elements. It has the advantages of simple structure, easy adjustment, and high spectral coverage, which is an effective way to improve the detection sensitivity of gas sensing systems such as tunable diode laser absorption spectroscopy. This invited paper summarizes the design theory and the research results of some mainstream types of MPCs based on two mirrors and more than two mirrors in recent years, and briefly introduces the application of some processed products. The design theory of modified ABCD matrix and vector reflection principle are explained in detail. Finally, trends in its development are predicted.

Keywords: multipass cell; tunable diode laser absorption spectroscopy; gas sensing; optical path length.

DOI: 10.3788/COL202321.033001

1. Introduction

Gas sensing technology is a kind of measurement technique with a wide range of applications. The gas sensing technology based on optical principles has some significant advantages, such as high sensitivity, high selectivity, and fast response[1–9]. It has very important research and application value in the fields of atmospheric environmental monitoring, combustion diagnosis, fire warning, life medicine, etc.[10–13]. For example, in the field of environmental monitoring, the measurement of greenhouse gases such as methane and carbon dioxide as well as harmful gases such as nitrogen oxides and sulfur oxides in the atmosphere is of great significance for environmental protection[14–16]. In the field of fire warning, carbon monoxide, carbon dioxide, hydrogen, and other gases are usually produced in the early stage of fire. The measurement of these products can analyze the mechanism of fire formation and give early warnings of fire[17–19].

The optical gas sensing methods can be divided into three main types: 1) direct absorption spectroscopy, such as tunable diode laser absorption spectroscopy (TDLAS)[20–22]; 2) cavity-enhanced absorption spectroscopy (CEAS)[23,24]; 3) indirect absorption spectroscopy, such as photoacoustic spectroscopy (PAS) and light-induced thermoelastic spectroscopy (LITES)[25–29]. Compared with CEAS and indirect absorption spectroscopy, TDLAS has the merits of a compact structure and simple setup. Therefore, it is one of the most used techniques in gas sensing applications. It can provide a fast response, high sensitivity, reliable real-time and noncontact measurement[30,31]. A typical TDLAS system consists of three parts: a tunable diode laser, a gas absorption cell, and a photodetector. According to the absorption signal of the gas collected by the photodetector, the characteristics of gas concentration and temperature can be reflected. The basic principle of TDLAS is the Beer–Lambert's law, which is shown in Eq. (1), where I_t and I_0 represent the laser intensity before and after gas absorption, α represents the absorption coefficient, and L represents the optical path length of gas absorption. It is obvious that the absorption signal can be effectively increased by simply increasing the absorption optical path length L of the gas while other conditions remain unchanged. Therefore, increasing the optical path of gas absorption can improve the detection performance and obtain a better minimum detection limit (MDL),

$$I_t = I_0 \exp(-\alpha L). \tag{1}$$

The research on the gas absorption cell has a long history, but up to now, the innovative research results on its structure and performance are still emerging endlessly. The most common method is to use different types of mirrors to constrain the incident beam and make it be reflected repeatedly in the gas absorption cell to increase the absorption path. This type of gas absorption cell is called a multipass cell (MPC). It has the advantages of simple structure, wide wavelength coverage, and suitability for a variety of gas sensing systems, and therefore, it is widely used[32,33]. There is also another type of gas absorption cell made of hollow optic fibers[34,35]. But its production process is not mature, and the optical loss is high, especially in the long wavelength region. Hence, the mainstream use of gas absorption cell type is the MPC.

The use of MPC enables the incident beam to obtain a long absorption path in a small space, which is the key way to realize a highly sensitive and compact TDLAS-based gas sensor[36–42]. In recent years, researchers have optimized the MPC design from the types, quantities, and placement of mirrors, which effectively improved the utilization rate of MPC mirrors and promoted the further development of related gas sensing technology. This paper summarized the design progress of mainstream MPC, studied its practical application in gas sensing technology, and put forward the future development prospects.

2. Design of the MPC Consisting of Two Mirrors

The most classical MPC can be constructed by using two mirrors placed in parallel. In 1962, Herriott *et al.*[43,44] at Bell Laboratories designed the Herriott cell using two identical concave spherical mirrors. Based on this, researchers have successively designed the astigmatic mirror cell and the dense spot pattern MPC. However, the first two types have some obvious disadvantages. The spot pattern of the Herriott cell is shown in Fig. 1(a); the spot usually forms a circle or ellipse on the mirror. This type of spot distribution leads to low utilization of spherical mirrors. In 2018, Zheng *et al.*[45] from Jilin University improved the Herriott cell and designed a dual-path Herriott cell, which is shown in Fig. 1(b). This approach does not fundamentally solve the problem of low utilization of the mirror. The spot pattern of the astigmatic mirror cell is shown in Fig. 1(c); the pattern of specular spot distribution is a Lissajous pattern. Due to the high processing cost and difficulties with the aspherical mirror, the development of aspherical mirror cells is very limited. The dense spot pattern MPC inherits the advantages of high stability and easy adjustment of the Herriott cell, and the use of a concave spherical mirror can significantly improve the utilization rate of the mirror and increase the absorption path. Therefore, the following will introduce the related design research results.

2.1. Design method of MPC composed of double spherical mirrors based on a modified ABCD matrix

For the Herriott cell, the reflection behavior of laser between two spherical mirrors can be described by the light propagation ABCD matrix[47], as shown in Eq. (2). As an improved version of the Herriott cell, the most important feature of the dense spot-pattern-based MPC is that the laser reflected between the two spherical mirrors is mostly off-axis, which no longer meets the paraxial approximation condition, so the mentioned matrix in Eq. (2) is no longer applicable,

$$\begin{bmatrix} A & B \\ C & D \end{bmatrix} = \begin{bmatrix} 1 & 0 \\ -\frac{2}{R} & 1 \end{bmatrix} \cdot \begin{bmatrix} 1 & D \\ 0 & 1 \end{bmatrix}. \tag{2}$$

In 2019, Cui *et al.*[48] proposed a theoretical calculation model based on the modified ABCD matrix that fully considered the influence of spherical mirror phase difference on the design of the MPC. They corrected the paraxial approximation error in the matrix of Eq. (2) by introducing two new operators, S and L, which are $S_\varphi = \sin\varphi$ and $L_\varphi = -2\arcsin(\varphi/R)$, respectively, where φ is an arbitrary rational number. The modified matrix is shown in Eq. (3). When the beam incidence parameters (including the position coordinates and the angles) are set well, the beam between mirrors can be accurately tracked according to the above model, and then the reasonable design parameters of a dense spot-type-based MPC can be obtained. In addition, the calculation results of the above model are in good agreement with the simulation results of the optical software TracePro. Some calculation and simulation results are shown in Fig. 2. According to the simulation results, these dense spot-pattern-based MPCs have a smaller volume and larger mirror utilization compared with the traditional Herriott cell,

$$\begin{bmatrix} A & B \\ C & D \end{bmatrix} = \begin{bmatrix} 1 & 0 \\ L & 0 \end{bmatrix} \cdot \begin{bmatrix} 1 & d_n S \\ 0 & 1 \end{bmatrix}. \tag{3}$$

However, it is not accurate to use only ideal lines and points to describe the beam and the spots on mirrors. In 2020,

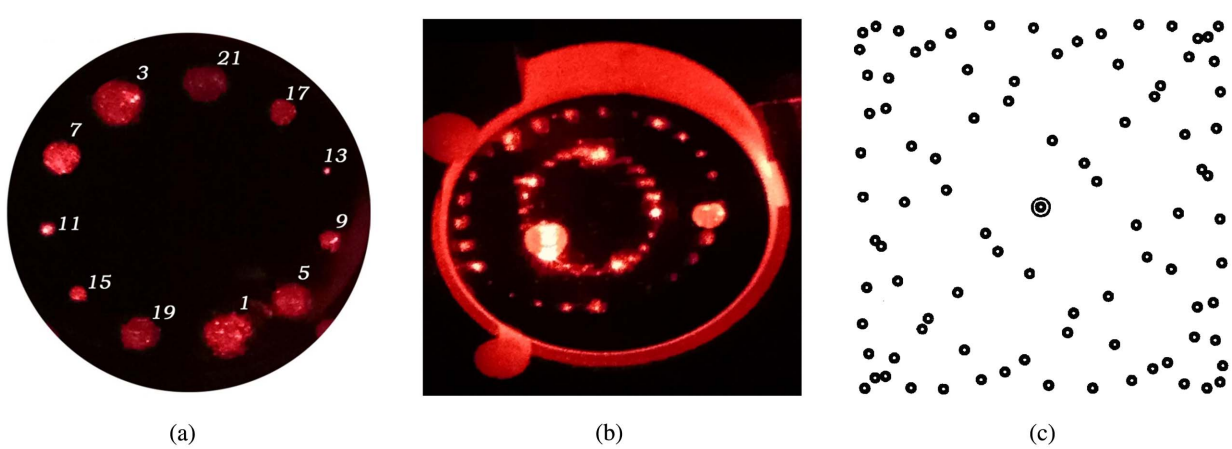

Fig. 1. Spot patterns of different kinds of MPCs consisting of two mirrors. (a) Spot pattern of a Herriott cell[32]; (b) spot pattern of a dual-path Herriott cell[32]; (c) spot pattern of the astigmatic mirror cell[46].

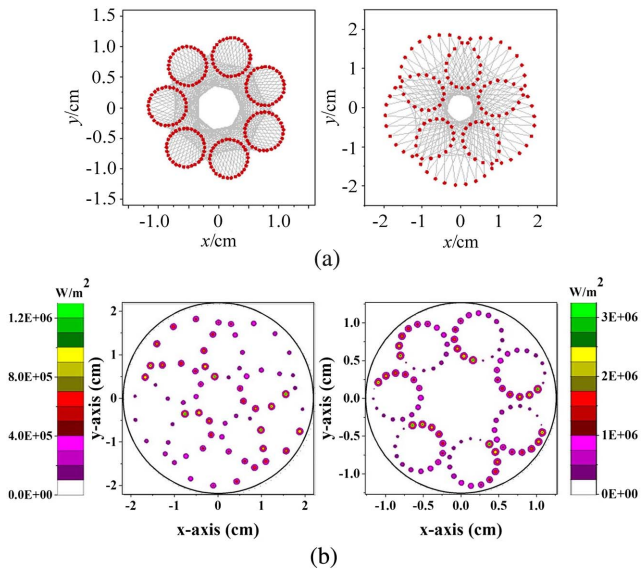

Fig. 2. Model calculation and TracePro simulation of spot distribution pattern of an MPC consisting of double spherical mirrors. (a) Dense spot pattern gotten by the calculation model; (b) spot pattern simulated by TracePro with the same parameters as in (a). Reprinted with permission from Ref. [48] © Optica Publishing Group.

Cui *et al.*[40,49] optimized the previous calculation model, expanding single-ray tracing to multiple-ray tracing so that the shape of the spot on the spherical mirror could be calculated. The optimized model fully considers the influence of spherical aberration and astigmatism and can provide effective theoretical guidance for avoiding the overlapping of some light spots in the design process of MPC with dense light spots. The specular spot distribution diagram simulated by the above model and the real processing effect are shown in Fig. 3. Two spherical mirrors with a 50.8 mm diameter and 100 mm radius of curvature were used for the processing. The reflectivity of the mirror was 98%, and the shape and distribution of the spot were observed through a visible diode laser with a wavelength of 635 nm. In addition, in order to verify the performance of the designed MPC in the sensor system, the MPC with an eight-multicircle spot pattern in Fig. 3 was used to build a TDLAS methane sensor, and a distributed-feedback tunable diode laser with a wavelength of 1.65 μm was used to detect ambient methane (~1.8 ppm; ppm, parts per million). The signal-to-noise ratio of ~93 could be obtained by scanning the $2f$ spectrum.

2.2. Design method of MPC composed of double spherical mirrors based on the vector reflection principle

Although the error of paraxial approximation can be eliminated by using the modified ABCD matrix, complex matrix operation and iteration are required repeatedly in the actual ray-tracing process, which makes the design process very complicated. In 2020, Kong *et al.*[50] reported a design method for dense spot pattern MPC based on the vector reflection principle, which uses a more concise process in ray tracing. This theory represents the

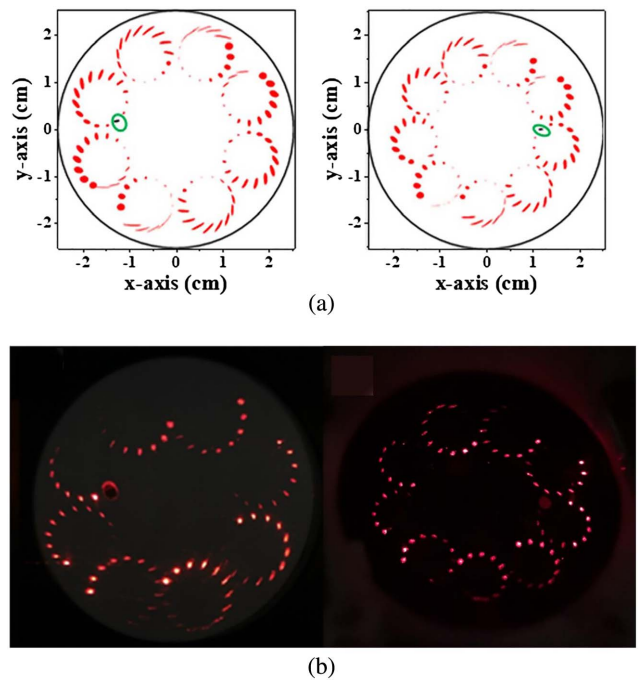

Fig. 3. Exotic spot patterns generated by an MPC consisting of double spherical mirrors. (a) Simulated results, and the black spots surrounded by the green circles represent the exit positions of the beam; (b) photographs of the real spot patterns on the exit spherical surfaces. Reproduced from Ref. [49], with the permission of AIP Publishing.

light reflected between two spherical mirrors in the form of a vector, and the direction of the vector is the direction vector of the beam. The magnitude of the vector is the propagation distance of the beam between the two adjacent reflections. The reflections of the beam on spherical mirrors are transformed into a vector calculation, and ray tracing is realized through the iterative relation in Eq. (4) to Eq. (6). r, r_f, and r_N represent the direction vectors of reflected light, incident light, and the normal, respectively; P_0 and P_1 represent the coordinates of reflected and incident points, respectively, and the superscript i represents the order of reflection,

$$r_f^{(i)} = r^{(i)} - (2r^{(i)} \cdot r_N^{(i)})r_N^{(i)}, \tag{4}$$

$$P_0^{(i+1)} = P_1^{(i)}, \tag{5}$$

$$r^{(i+1)} = r_f^{(i)}. \tag{6}$$

In 2021, based on the above theory, Liu *et al.*[52] reported an automatic approach to optimizing the MPC design with independent circle patterns. In this method, the distance between two mirrors is first determined by a Monte Carlo algorithm, and then the incident parameters are locally optimized by Nelder–Mead simplex algorithm. Similarly, multiray tracing is used to simulate the size and shape of the spot. Three independent circle patterns MPCs with five, seven, and nine circles were obtained by using this design method. In particular, the quality

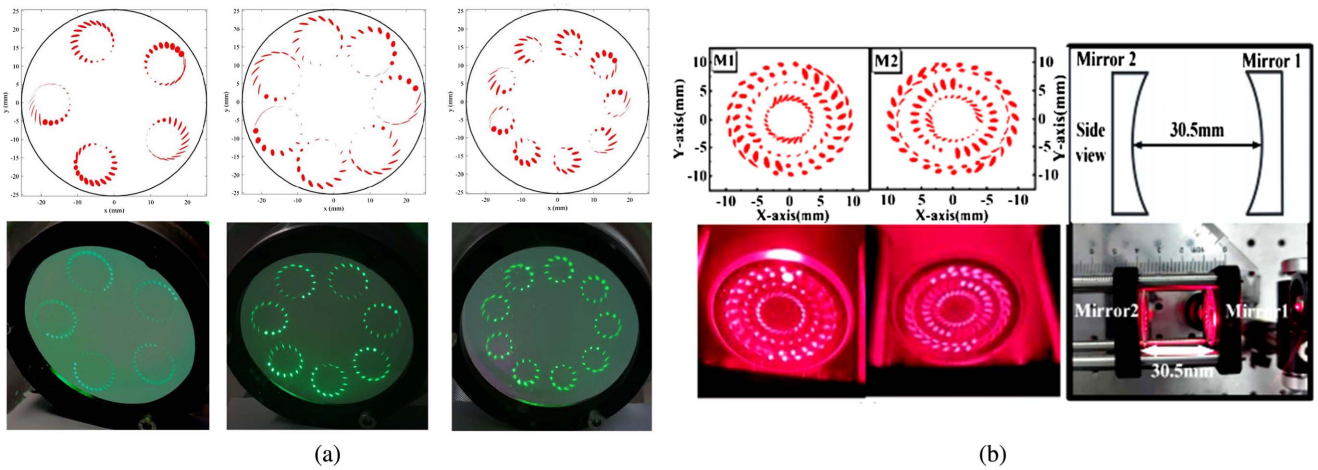

(a) (b)

Fig. 4. MPCs consisting of double spherical mirrors based on the vector reflection theory. (a) Three independent circle patterns-based MPCs with five, seven, and nine circles; those above are simulated patterns by using multiray tracing, while those below are the corresponding physical photographs. Reprinted with permission from Ref. [52] © Optica Publishing Group. (b) Simulated results and real photographs of MPC with high density[51].

of the output beam can be optimized by changing the incident point and converging the beam to the optimum point. The corresponding simulated results and physical photographs are shown in Fig. 4(a). The curvature radius and diameter of the spherical mirror are 100 and 50.8 mm, respectively. It is worth noting that when the number of reflections is similar, the designed MPC with independent circle patterns is stabler than the Herriott cell. According to this method, the independent-circle-patterns-based MPCs with better compactness and stability can be designed, which can effectively improve the detection sensitivity of a trace gas sensing system. The detailed parameters of the MPCs in Fig. 4 are shown in Table 1, where N represents the reflection times, and x, y, θ, and φ represent the incident position and angle, respectively. d represents the distance between the two mirrors, and OPL represents the optical path length. In 2022, Chen *et al.*[51] did a similar study, except that they used a parallel multipopulation genetic algorithm (PMPGA) to calculate the parameter configuration of the mirror. An MPC with an OPL of 6.3 m was produced, while the mirror diameter and two-mirror distance of only 25.4 and 30.5 mm were manufactured; such an MPC was validated by TDLAS method.

The dense spot-pattern-based MPCs proposed above are all based on the structure of two spherical mirrors placed parallel to the common axis. In a sense, it is the result of the optimization of some parameters of the Herriott cell; the most significant difference is that the Herriott cell requires a smaller angle of incidence. As the number of reflections increases, the spots on the mirrors are varied, so we need to use the two theories mentioned above to track the reflected beams more accurately. At the same time, parameter selection can be achieved more efficiently with the help of some algorithms. In general, a dense spot-pattern-based MPC significantly improves the OPL while retaining the advantages of high stability and easy adjustment, and can cover a wide wavelength range by coating the mirror with various highly reflective materials (most are gold or silver).

3. Design of the MPC Consisting of More than Two Mirrors

Although the utilization of the spherical mirror has been greatly improved from the Herriott cell to the dense spot-pattern-based MPC, there is still some room for improvement compared with the spot distribution of the astigmatic mirror in Fig. 1(c). Increasing the number of mirrors or using different types of mirrors can bring more possibilities to the design of an MPC. In fact, the earliest MPC (the White cell) consisted of three concave

Table 1. Parameters of the Spot Patterns in Fig. 4.

Pattern	N	x (mm)	y (mm)	θ (°)	φ (°)	d (mm)	OPL (m)
Fig. 4(a) top left	210	10.38	15.27	1.45	−8.81	131.76	27.67
Fig. 4(a) top middle	210	15.29	9.48	−0.80	−7.91	123.07	25.84
Fig. 4(a) top right	198	11.62	12.82	0.42	−9.95	118.37	23.44
Fig. 4(b)	212	1.2	8.1	6.7	−1.1	30.5	6.3

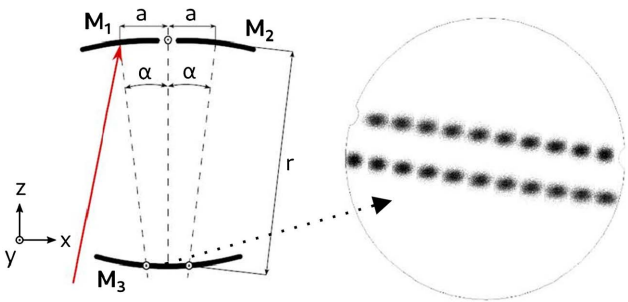

Fig. 5. Structure of a White cell and the spot pattern on M3. Reprinted with permission from Ref. [55] © Optica Publishing Group.

spherical mirrors with the same radius of curvature and placed in specific positions[53,54], as shown in Fig. 5. The conjugate focus structure of the White cell makes the beam be reflected between the mirrors many times, so as to achieve the purpose of increasing the absorption path, and the light spots on the mirror show regular array distribution. The MPC with a larger number of mirrors is more flexible and adaptable to complex measurement environments, so the results of the research on MPC consisting of more than two mirrors are presented in the following.

3.1. Design of bow-tie-like MPC based on genetic algorithm optimization

In 2021, Arkadiusz *et al.*[55] reported a method to design an MPC with at least three ordinary spherical mirrors. By designing the mirror position and angle, using ordinary spherical mirrors, they obtained a similar Lissajous pattern to that on the astigmatic cell. The most notable feature of this design method is the broken symmetry of the placement of the plane mirrors, which is the reason for the Lissajous pattern. As the number of mirrors increases, the reflection path of the beams among mirrors becomes more complex. The more possible path forms can be obtained with the increased mirrors. In general, beam path types can be divided into two types: rotating (when a laser beam is reflected by each mirror one by one) and returning (when a laser beam is reflected back at the last mirror). The schematic diagram is shown in Fig. 6(a). The returning structure has a larger OPL-to-volume ratio (OPL/V, which is used to quantitatively describe the compactness of the MPC) and is more suitable for finding the optimal configuration.

Considering the complexity of the design, a bow-tie-like MPC with four spherical mirrors based on the above theory was designed and processed. The beam path type follows the returning structure shown in panel d) in Fig. 6(a). The numerical simulation part is implemented by a C++ program. The principle of ray tracing is the vector reflection theory mentioned above. The authors used a genetic algorithm to find the configuration parameters of the MPC. The diameter and focal length of the spherical mirror were set as 25 mm, and the aperture of the input and output holes was 3 mm, which was located in the center of the input mirror. The designed configuration with 16 and 23.8 m OPLs was obtained; the structure is shown in Fig. 6(b). The actual OPLs of the MPC were measured by the time-of-flight (TOF) method[56], which were 16.1 and 23.9 m, respectively, within the error range. They have also been well validated in TDLAS-based direct absorption and wavelength modulation spectroscopy. In addition to its excellent compactness and stability, the most attractive advantage of this design is the use of relatively inexpensive standard spherical mirrors to achieve the mirror utilization of astigmat-based MPC.

In 2022, Cheng *et al.*[57] did similar work and designed a folded MPC using three spherical mirrors. The structure of the MPC is shown in Fig. 7. The mirrors have a noncoaxial V-shaped distribution, and the entry hole of the beam is also its exit hole. It is worth noting that the theory of ABCD matrix is used for the ray tracing in the numerical simulation of this folded MPC. Because its structure is very similar to the folded cavity in the laser cavity, the reflection of the beam can be equivalent to the transmission in the equivalent coaxial structure, so the beam propagation matrix can be used for simulation and design. Finally, three effective OPLs of 49.6, 97.6, and 173.6 m were obtained.

3.2. Design of MPC based on circular prism array

The MPCs mentioned above are all close-type, and in practical application, it is necessary to use the means of bypass extraction

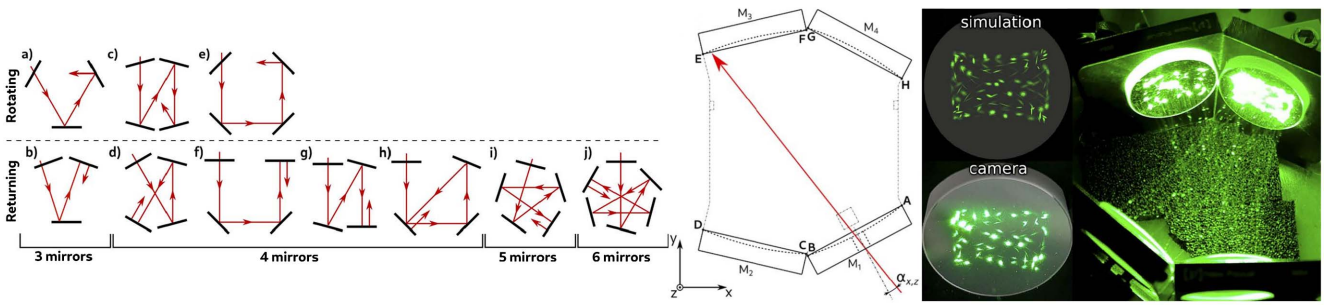

(a) (b)

Fig. 6. MPC based on at least three spherical mirrors. (a) Beam path types in MPC based on three to six spherical mirrors; (b) structural drawings and physical photographs (the OPL is 23.8 m) of bow-tie-like MPC based on four spherical mirrors. Reprinted with permission from Ref. [55] © Optica Publishing Group.

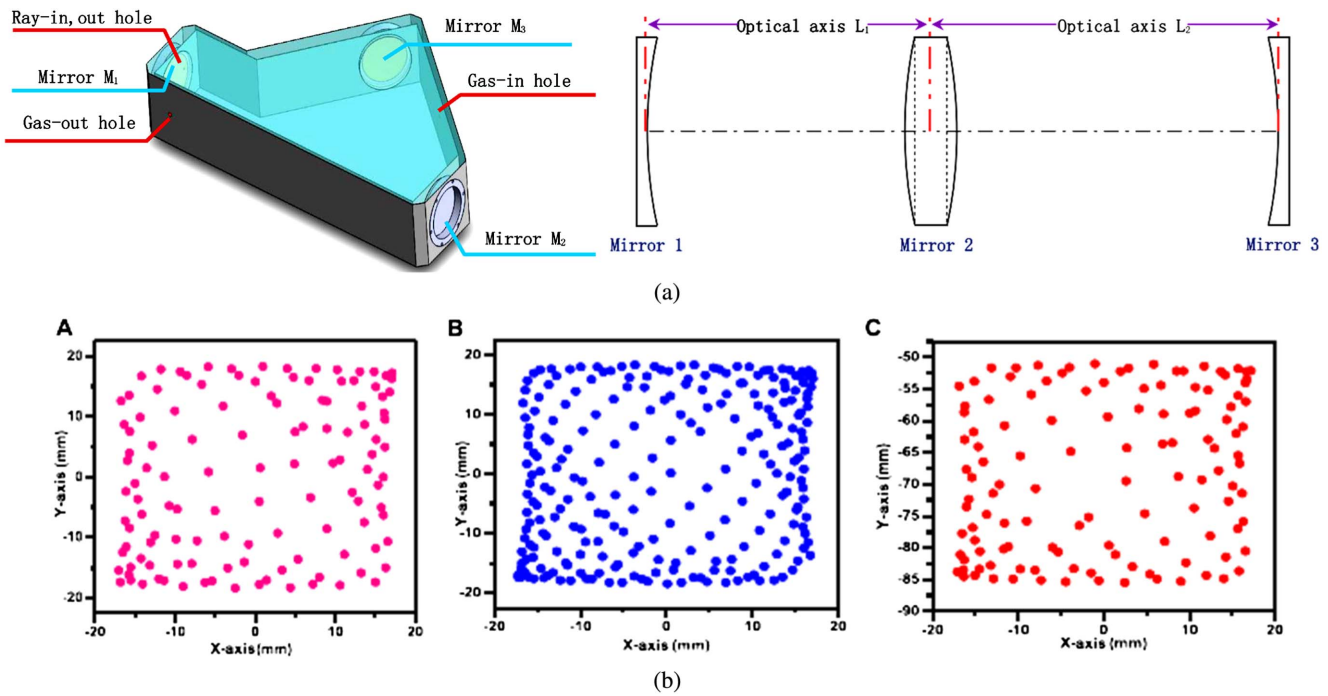

Fig. 7. Folded MPC consisting of three spherical mirrors with off-axis placement. (a) Structure of MPC and its equivalent coaxial structure; (b) simulated results of mirror spot of the folded MPC with OPL of 97.6 m[57].

for gas detection. Although high detection sensitivity can be obtained in this way, due to the influence of additional pump suction force and long-term continuous measurement, the gas state inside an MPC may still be inconsistent with the actual gas environment, which leads to measurement errors and is not conducive to transient monitoring. For example, the oil and gas industry uses a very important step to realize *in situ* detection of water vapor in pipelines. In similar application scenarios, the open-type MPC has the advantage of being able to detect the transient characteristics of the gas inside the pipeline.

In 2021, Wang *et al.*[58] reported the design and application of an MPC based on a novel circular prism array (CPA-MPC). This design is inspired by the cyclic MPC (C-MPC), which was first proposed by Thoma *et al.*[59]. The biggest difference between the CPA-MPC and the C-MPC lies in the use of a prism array instead of a curved mirror, which has the advantage of avoiding the astigmatism of the beam caused by multiple off-axis reflection between the curved mirrors. The beam astigmatism will produce strong optical fringe noise to the measured signal. The beam transmission path in CPA-MPC conforms to the principle of the Euler graph. The beam is shot at a certain angle to the prisms distributed in circular arrays, and then propagates along the one-stroke star-polygon pattern. After being reflected by the last prism, it is received by the photodetector. Considering the optical path of gas absorption and the difficulty of optical alignment, an optimal optical path scheme is obtained based on a fuzzy comprehensive evaluation method. Finally, the 12-star polygon was determined as the best optical path, and the absorption OPL of 173.9 cm was achieved in the ring volume of 217 mL. The structure of the MPC is shown in Fig. 8. Using this CPA-MPC to build a water vapor sensor, the signal-to-noise ratio reached 608.3, which is 13 times higher than that of the traditional opposite-type laser detection method. Although the OPL of a CPA-MPC is much shorter than that of other types of MPCs, the advantages of the CPA-MPC in specific application scenarios are irreplaceable, which also shows that MPC design with multiple mirrors has more possibilities and flexibility.

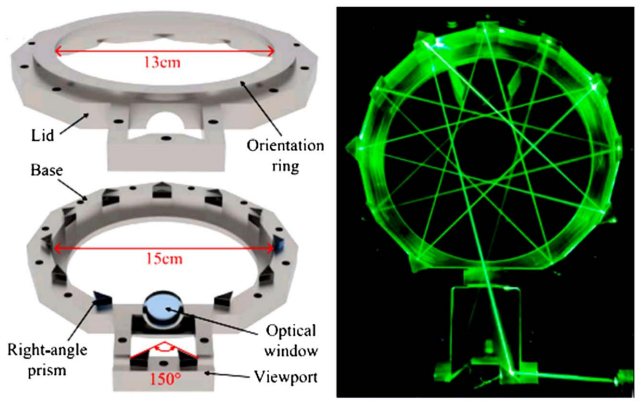

Fig. 8. Circular prism array MPC: on the left is a detailed view of the object; on the right is a photograph of the optical path pattern observed using a 532 nm visual laser[58].

By increasing the number of mirrors or changing the type of mirrors, more reflective types of MPC structures are indeed obtained. Meanwhile, the difficulty of obtaining the design parameters is also greatly increased, and this is because the

reflection behavior of beams is influenced by multiple parameters. Moreover, in terms of ray tracing, the vector reflection principle shows greater advantages because it does not need to adjust the beam transmission matrix according to the placement of the mirrors.

4. Conclusion

With the development of light tracing theories and methods, MPC, as a core element of the TDLAS technique, has been researched widely in recent years. Numerical simulation is becoming more and more important for the design of an MPC with various singular spot patterns, and the MPC develops in the direction of having a longer absorption path, more compact structure, higher mirror utilization, higher stability, better robustness, lower cost, and broader application. This paper summarized the innovative design types and research progress of some representative MPCs in recent years. From the perspective of the number of mirrors used, the design theories and experimental results of various MPCs are introduced, and their advantages and disadvantages are analyzed. Despite its rapid development, it still needs further research to achieve large-scale application. Its future development direction can refer to the following points: (1) for the MPC consisting of multiple mirrors, attention should be paid to the flexibility of design, and the MPC design method with free and adjustable optical path should meet different measurement requirements; (2) improve its miniaturization, light weight, and stability, so as to adapt to the special platform such as unmanned aerial vehicle (UAV); (3) for the existing design types, the combination with other technologies such as light-induced thermoelastic spectroscopy (LITES) is considered to achieve a high detection sensitivity[38,60–62].

Acknowledgement

This work was supported by the National Natural Science Foundation of China (Nos. 62275065, 62022032, and 61875047), Natural Science Foundation of Heilongjiang Province of China (No. YQ2019F006), and Fundamental Research Funds for the Central Universities.

References

1. Z. Zhang, F. Zhang, B. Xu, H. Xie, B. Fu, X. Lu, N. Zhang, S. Yu, J. Yao, and Y. Cheng, "High-sensitivity gas detection with air-lasing-assisted coherent Raman spectroscopy," Ultrafast Science **2022**, 9761458 (2022).
2. Y. Hu, S. Qiao, Z. Lang, Y. He, and Y. Ma, "Quartz-enhanced photoacoustic-photothermal spectroscopy for trace gas sensing," Opt. Express **29**, 5121 (2021).
3. Y. Fu, J. Cao, K. Yamanouchi, and H. Xu, "Air-laser-based standoff coherent Raman spectrometer," Ultrafast Science **2022**, 9867028 (2022).
4. Y. Ma, Y. He, Y. Tong, X. Yu, and F. K. Tittel, "Quartz-tuning-fork enhanced photothermal spectroscopy for ultra-high sensitive trace gas detection," Opt. Express **26**, 32103 (2018).
5. Z. Lang, S. Qiao, Y. He, and Y. Ma, "Quartz tuning fork-based demodulation of an acoustic signal induced by photo-thermo-elastic energy conversion," Photoacoustics **22**, 100272 (2021).
6. R. Rousseau, Z. Loghmari, M. Bahriz, K. Chamassi, R. Teissier, A. N. Baranov, and A. Vicet, "Off-beam QEPAS sensor using an 11-μm DFB-QCL with an optimized acoustic resonator," Opt. Express **27**, 7435 (2019).
7. S. Qiao, Y. He, and Y. Ma, "Trace gas sensing based on single-quartz-enhanced photoacoustic-photothermal dual spectroscopy," Opt. Lett. **46**, 2449 (2021).
8. Q. Wang, Z. Wang, W. Ren, P. Patimisco, A. Sampaolo, and V. Spagnolo, "Fiber-ring laser intracavity QEPAS gas sensor using a 7.2 kHz quartz tuning fork," Sens. Actuators B Chem. **268**, 512 (2018).
9. Y. Ma, Y. Hu, S. Qiao, Z. Lang, X. Liu, Y. He, and V. Spagnolo, "Quartz tuning forks resonance frequency matching for laser spectroscopy sensing," Photoacoustics **25**, 100329 (2022).
10. R. Ghorbani and F. M. Schmidt, "Real-time breath gas analysis of CO and CO_2 using an EC-QCL," Appl. Phys. B **123**, 1432 (2017).
11. Y. He, Y. Ma, Y. Tong, X. Yu, and F. K. Tittel, "HCN ppt-level detection based on a QEPAS sensor with amplified laser and a miniaturized 3D-printed photoacoustic detection channel," Opt. Express **26**, 9666 (2018).
12. E. Lellouch, M. Gurwell, B. Butler, T. Fouchet, P. Lavvas, D. Strobel, B. Sicardy, A. Moullet, R. Moreno, and D. Bockelée-Morvan, "Detection of CO and HCN in Pluto's atmosphere with ALMA," ICARUS **286**, 289 (2017).
13. Y. Ma, Y. He, L. Zhang, X. Yu, J. Zhang, R. Sun, and F. K. Tittel, "Ultra-high sensitive acetylene detection using quartz-enhanced photoacoustic spectroscopy with a fiber amplified diode laser and a 30.72 kHz quartz tuning fork," Appl. Phys. Lett. **110**, 031107 (2017).
14. X. Liu, S. Qiao, and Y. Ma, "Highly sensitive methane detection based on light-induced thermoelastic spectroscopy with a 2.33 μm diode laser and adaptive Savitzky-Golay filtering," Opt. Express **30**, 1304 (2022).
15. Y. Ma, R. Lewicki, M. Razeghi, and F. K. Tittel, "QEPAS based ppb-level detection of CO and N_2O using a high power CW DFB-QCL," Opt. Express **21**, 1008 (2013).
16. L. Hu, C. Zheng, M. Zhang, K. Zheng, J. Zheng, Z. Song, X. Li, Y. Zhang, Y. Wang, and F. K. Tittel, "Long-distance in-situ methane detection using near-infrared light-induced thermo-elastic spectroscopy," Photoacoustics **21**, 100230 (2021).
17. Y. Ma, Y. Hu, S. Qiao, Y. He, and F. K. Tittel, "Trace gas sensing based on multi-quartz-enhanced photothermal spectroscopy," Photoacoustics **20**, 100206 (2020).
18. A. Kosterev, F. Tittel, and G. Bearman, "Advanced quartz-enhanced photoacoustic trace gas sensor for early fire detection," SAE Int. J. Aerosp. **1**, 331 (2008).
19. B. Su, Z. Luo, T. Wang, and L. Liu, "Experimental and numerical evaluations on characteristics of vented methane explosion," J. Cent. South Univ. **27**, 2382 (2020).
20. X. Liu and Y. Ma, "Tunable diode laser absorption spectroscopy based temperature measurement with a single diode laser near 1.4 μm," Sensors **22**, 6095 (2022).
21. S. Bürkle, L. Biondo, C.-P. Ding, R. Honza, V. Ebert, B. Böhm, and S. Wagner, "In-cylinder temperature measurements in a motored IC engine using TDLAS," Flow Turbul. Combust. **101**, 139 (2018).
22. C. Liu, L. Xu, J. Chen, Z. Cao, Y. Lin, and W. Cai, "Development of a fan-beam TDLAS-based tomographic sensor for rapid imaging of temperature and gas concentration," Opt. Express **23**, 22494 (2015).
23. X. Zhou, G. Zhao, J. Liu, Y. Zhou, X. Yan, Z. Li, W. Ma, and S. Jia, "Fiber pigtailed DFB laser-based optical feedback cavity enhanced absorption spectroscopy with a fiber-coupled EOM for phase correction," Opt. Express **30**, 6332 (2022).
24. K. Zheng, C. Zheng, Y. Zhang, Y. Wang, and F. K. Tittel, "Review of incoherent broadband cavity-enhanced absorption spectroscopy (IBBCEAS) for gas sensing," Sensors **18**, 3646 (2018).
25. Y. Ma, W. Feng, S. Qiao, Z. Zhao, S. Gao, and Y. Wang, "Hollow-core anti-resonant fiber based light-induced thermoelastic spectroscopy for gas sensing," Opt. Express **30**, 18836 (2022).
26. X. Liu and Y. Ma, "Sensitive carbon monoxide detection based on light-induced thermoelastic spectroscopy with a fiber-coupled multipass cell," Chin. Opt. Lett. **20**, 031201 (2022).

27. K. Liu, J. Mei, W. Zhang, W. Chen, and X. Gao, "Multi-resonator photoacoustic spectroscopy," Sens. Actuators B Chem **251**, 632 (2017).
28. Z. Gong, G. Wu, X. Jiang, H. Li, T. Gao, M. Guo, F. Ma, K. Chen, L. Mei, W. Peng, and Q. Yu, "All-optical high-sensitivity resonant photoacoustic sensor for remote CH_4 gas detection," Opt. Express **29**, 13600 (2021).
29. P. Patimisco, A. Sampaolo, L. Dong, F. K. Tittel, and V. Spagnolo, "Recent advances in quartz enhanced photoacoustic sensing," Appl. Phys. Rev. **5**, 011106 (2018).
30. K. Krzempek, G. Dudzik, and K. Abramski, "Photothermal spectroscopy of CO_2 in an intracavity mode-locked fiber laser configuration," Opt. Express **26**, 28861 (2018).
31. T. Liang, S. Qiao, X. Liu, and Y. Ma, "Highly sensitive hydrogen sensing based on tunable diode laser absorption spectroscopy with a 2.1 μm diode laser," Chemosensors **10**, 321 (2022).
32. M. Dong, C. Zheng, Y. Zhang, Y. Wang, and F. K. Tittel, "Herriott cell design with minimum volume and multiple reflection rings for infrared gas sensing," IEEE Photon. Technol. Lett. **31**, 541 (2019).
33. M. Graf, L. Emmenegger, and B. Tuzson, "Compact, circular, and optically stable multipass cell for mobile laser absorption spectroscopy," Opt. Lett. **43**, 2434 (2018).
34. W. Feng, Y. Qu, Y. Gao, and Y. Ma, "Advances in fiber-based quartz enhanced photoacoustic spectroscopy for trace gas sensing," Microwave Opt. Technol. Lett. **63**, 2031 (2021).
35. L. Hu, C. Zheng, Y. Zhang, J. Zheng, Y. Wang, and F. K. Tittel, "Compact all-fiber light-induced thermoelastic spectroscopy for gas sensing," Opt. Lett. **45**, 1894 (2020).
36. K. Krzempek, M. Jahjah, R. Lewicki, P. Stefański, S. So, D. Thomazy, and F. K. Tittel, "CW DFB RT diode laser-based sensor for trace-gas detection of ethane using a novel compact multipass gas absorption cell," Appl. Phys. B **112**, 461 (2013).
37. R. Claps, F. V. Englich, D. P. Leleux, D. Richter, F. K. Tittel, and R. F. Curl, "Ammonia detection by use of near-infrared diode-laser-based overtone spectroscopy," Appl. Opt. **40**, 4387 (2001).
38. Y. He, Y. Ma, Y. Tong, X. Yu, and F. K. Tittel, "Ultra-high sensitive light-induced thermoelastic spectroscopy sensor with a high *Q*-factor quartz tuning fork and a multipass cell," Opt. Lett. **44**, 1904 (2019).
39. H. Chen, C. Chen, Y. Wang, H. Piao, and P. Wang, "Optical design and verification of multipass cell with two spherical mirrors using space equation method," IEEE Trans. Instrum. Meas. **70**, 7002808 (2021).
40. R. Cui, L. Dong, H. Wu, W. Ma, L. Xiao, S. Jia, W. Chen, and F. K. Tittel, "Three-dimensional printed miniature fiber-coupled multipass cells with dense spot patterns for ppb-level methane detection using a near-IR diode laser," Anal. Chem. **92**, 13034 (2020).
41. M. Mangold, B. Tuzson, M. Hundt, J. Jágerská, H. Looser, and L. Emmenegger, "Circular paraboloid reflection cell for laser spectroscopic trace gas analysis," J. Opt. Soc. Am. A **33**, 913 (2016).
42. B. Fang, N. Yang, W. Zhao, C. Wang, W. Zhang, W. Song, D. S. Venables, and W. Chen, "Improved spherical mirror multipass-cell-based interband cascade laser spectrometer for detecting ambient formaldehyde at parts per trillion by volume levels," Appl. Opt. **58**, 8743 (2019).
43. D. R. Herriott and H. J. Schulte, "Folded optical delay lines," Appl. Opt. **4**, 883 (1965).
44. D. Herriott, H. Kogelnik, and R. Kompfner, "Off-axis paths in spherical mirror interferometers," Appl. Opt. **3**, 523 (1964).
45. W. Ye, M. Dong, S. Miao, C. Zheng, Y. Wang, F. K. Tittel, D. Yao, and G. Zhong, "Double-range near-infrared acetylene detection using a dual spot-ring Herriott cell (DSR-HC)," Opt. Express **26**, 12081 (2018).
46. J. B. McManus, P. L. Kebabian, and M. S. Zahniser, "Astigmatic mirror multipass absorption cells for long-path-length spectroscopy," Appl. Opt. **34**, 3336 (1995).
47. Y. N. Cao, Z. Xu, X. Tian, G. Cheng, C. L. Liu, and Y. L. Zhang, "Generalized calculation model of different types of optical multi-pass cells based on refraction and reflection law," Opt. Laser Technol. **139**, 106958 (2021).
48. R. Cui, L. Dong, H. Wu, S. Li, X. Yin, L. Zhang, W. Ma, W. Yin, and F. K. Tittel, "Calculation model of dense spot pattern multi-pass cells based on a spherical mirror aberration," Opt. Lett. **44**, 1108 (2019).
49. R. Cui, L. Dong, H. Wu, W. Chen, and F. K. Tittel, "Generalized optical design of two-spherical-mirror multi-pass cells with dense multi-circle spot patterns," Appl. Phys. Lett. **116**, 091103 (2020).
50. R. Kong, T. Sun, P. Liu, and X. Zhou, "Optical design and analysis of a two-spherical-mirror-based multipass cell," Appl. Opt. **59**, 1545 (2020).
51. H. Chen, C. Chen, and Y. Wang, "Auto-design of multi-pass cell with small size and long optical path length using parallel multi-population genetic algorithm," IEEE Sens. J. **22**, 6518 (2022).
52. J. Liu, Y. Chen, L. Xu, R. Kong, P. Liu, and X. Zhou, "Generalized optical design and optimization of multipass cells with independent circle patterns based on the Monte Carlo and Nelder-Mead simplex algorithms," Opt. Express **29**, 20250 (2021).
53. H. M. Pickett, G. M. Bradley, and H. L. Strauss, "A new white type multiple pass absorption cell," Appl. Opt. **9**, 2397 (1970).
54. H. J. Bernstein and G. Herzberg, "Rotation-vibration spectra of diatomic and simple polyatomic molecules with long absorbing paths. I. The spectrum of fluoroform (CHF_3) from 2.4μ to 0.7μ," J. Chem. Phys. **16**, 30 (1948).
55. A. Hudzikowski, A. Głuszek, K. Krzempek, and J. Sotor, "Compact, spherical mirror-based dense astigmatic-like pattern multipass cell design aided by a genetic algorithm," Opt. Express **29**, 26127 (2021).
56. A. Hudzikowski, A. Gluszek, K. Krzempek, and J. Sotor, "Spherical mirrors based compact multipass cell with dense astigmatic-like spot pattern," in *Conference on Lasers and Electro-Optics* (2019), paper AF2K.8.
57. G. Cheng, Y.-N. Cao, X. Tian, J.-J. Chen, and J.-J. Wang, "Design and analysis of novel folded optical multi-pass cell," Front. Phys. **10**, 907715 (2022).
58. M. Wang, D. Wang, Y. Lv, P. Li, D. Li, and Y. Li, "*In-situ* laser detection of water vapor based on circular prism array multi-pass cell enhanced near-infrared absorption spectroscopy," Infrared Phys. Technol. **116**, 103811 (2021).
59. M. L. Thoma, R. Kaschow, and F. J. Hindelang, "A multiple-reflection cell suited for absorption measurements in shock tubes," Shock Waves **4**, 51 (1994).
60. S. Qiao, Y. Ma, Y. He, P. Patimisco, A. Sampaolo, and V. Spagnolo, "Ppt level carbon monoxide detection based on light-induced thermoelastic spectroscopy exploring custom quartz tuning forks and a mid-infrared QCL," Opt. Express **29**, 25100 (2021).
61. S. Qiao, A. Sampaolo, P. Patimisco, V. Spagnolo, and Y. Ma, "Ultra-highly sensitive HCl-LITES sensor based on a low-frequency quartz tuning fork and a fiber-coupled multi-pass cell," Photoacoustics **27**, 100381 (2022).
62. Y. Ma, C. Zheng, L. Hu, K. Zheng, F. Song, Y. Zhang, Y. Wang, and F. K. Tittel, "High-robustness near-infrared methane sensor system using self-correlated heterodyne-based light-induced thermoelastic spectroscopy," Sens. Actuators B Chem. **370**, 132429 (2022).